Chinese Chemical Letters 37 (2026) 111523

Contents lists available at ScienceDirect

Chinese Chemical Letters

journal homepage: www.elsevier.com/locate/cclet

NIR-II PTT and PA agents achieved by engineering D-A-D structure based on aza-BODIPY for tumor treatment

Siyi Hu[a,1], Wenze Zhang[b,1], Zhigang Ni[a], Liang Tian[a], Jiangwei Tian[b,*], Hua Lu[a,*], Lizhi Gai[a,*]

[a] College of Material, Chemistry and Chemical Engineering, Key Laboratory of Organosilicon Chemistry and Material Technology, Ministry of Education, Hangzhou Normal University, Hangzhou 311121, China
[b] State Key Laboratory of Natural Medicines, Jiangsu Key Laboratory of TCM Evaluation and Translational Research, China Pharmaceutical University, Nanjing 211198, China

ARTICLE INFO

Article history:
Received 2 May 2025
Revised 26 June 2025
Accepted 27 June 2025
Available online 27 June 2025

Keywords:
Aza-BODIPY
J-aggregation
NIR-II absorption
Photothermal therapy
Photoacoustic imaging

ABSTRACT

Near-infrared II (NIR-II) absorbing dye have garnered significant attention for deep-tissue tumor phototherapy and photoacoustic (PA) imaging. However, NIR-II dyes often suffer from poor photostability due to extensive conjugated systems, and J-aggregation type typically exhibit narrow absorption spectra, posing significant challenges in matching laser wavelengths. In this work, we propose a mechanism where charge transfer (CT)-type J aggregation, driven by enhanced intramolecular charge transfer, enables the broad NIR-II absorption peak and high photostability. The resulting dyes exhibit strong NIR-II absorption, low dark toxicity and high phototoxicity as well as improved biocompatibility. Upon 1064 nm excitation, BDP2-NPs achieve a photothermal conversion efficiency of 34.2 % and a maximum temperature of 47 °C, indicating moderate photothermal performance. In addition, PA imaging was assessed by different laser wavelength. This study underscores the potential of aza-boron-dipyrromethene (aza-BODIPY)-based dyes for developing advanced NIR-II agents in photothermal therapy and PA imaging.

© 2026 Published by Elsevier B.V. on behalf of Chinese Chemical Society and Institute of Materia Medica, Chinese Academy of Medical Sciences.

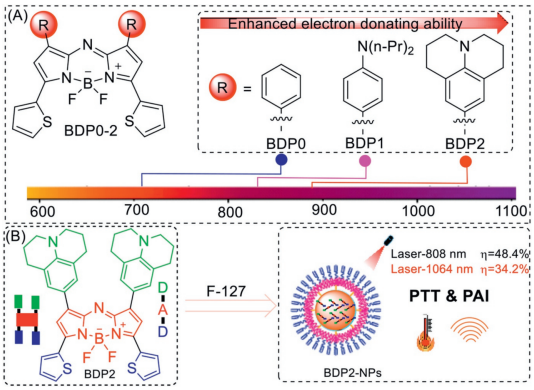
Over the past few decades, photoacoustic (PA) imaging has been widely utilized in clinical medicine and biomedical research due to its high image contrast, strong tissue penetration, and excellent resolution [1–4]. The technique works by using specific dyes that absorb light, causing a local thermal expansion that generates sound waves, which are then detected to form an image [2]. As the core energy transduction medium, optical absorbing dyes play a crucial role in PA imaging systems. Developing new PA agents with better light-to-sound efficiency, stability, and biocompatibility can improve PA imaging, making it more effective for applications in precision medicine, tumor diagnosis, vascular imaging, and neuroscience.

Near-infrared II (NIR-II, 1000–1700 nm) absorbing dyes are increasingly recognized for their potential applications in biophotonics, including biosensing, biomedicine, and bioimaging [5,6]. These dyes provide enhanced resolution and deeper tissue penetration (5–20 mm) over NIR-I dyes, due to reduced photon scattering, lower tissue absorption and minimal autofluorescence [7–17]. Their development is thus of great importance. A variety of NIR-II small molecules have been rapidly utilized for tumor imaging and photothermal therapy (PTT), including polymethine cyanines, xanthones, benzobisthiadiazoles, and boron-dipyrromethene (BODIPY) dyes [18–22]. Typically, the construction of NIR-II small molecules involves molecular engineering, supramolecular engineering, or a combination of both. The former includes strategies such as heteroatom substitution, conjugation extension, and D-A-D structures, while the latter involves the formation of J-aggregates. However, due to their large extended conjugated systems, NIR-II dyes usually exhibit poor photostability. Additionally, J-aggregates often have narrow absorption spectra, which makes it challenging to match the wavelengths of lasers.

Charge transfer (CT)-coupled J-aggregation, a method where donor-acceptor-donor (D-A-D) type dye molecules stack in an orderly fashion, induces a broad absorption peak due to strong coupling between the donor and acceptor units both within and between dyes [21]. Our research group has previously developed aza-BODIPY-based photothermal agents for tumor treatment [23], but their CT-coupled J-aggregation absorption was limited to the NIR-I region, reducing effectiveness in deep-tissue therapy. To over-

* Corresponding authors.
E-mail addresses: jwtian@cpu.edu.cn (J. Tian), hualu@hznu.edu.cn (H. Lu), lizhigai@hznu.edu.cn (L. Gai).
[1] These authors contributed equally to this work.

https://doi.org/10.1016/j.cclet.2025.111523
1001-8417/© 2026 Published by Elsevier B.V. on behalf of Chinese Chemical Society and Institute of Materia Medica, Chinese Academy of Medical Sciences.



Scheme 1. (A) Schematic diagram of the molecular design. (B) Preparation of BDP2-NPs with their PTT properties under different laser.

come this, we engineered a NIR-II dye, BDP2, by modifying the aniline component on the 3,5-dithiophene-aza-BODIPY core (Scheme 1). This design extends absorption into the NIR-II region with a broad shape and ordered aggregation is beneficial for enhancing photostability. After encapsulation with F-127, the absorption peak shifts to 914 nm, extending the absorption tail beyond 1100 nm. PA experiments confirm good tissue penetration, and biological tests demonstrate low toxicity, good biocompatibility, and high photothermal performance. This molecular design offers a promising pathway for developing NIR-II dyes based on aza-BODIPY, potentially advancing PTT for deep-seated tumors and contributing to the broader field of biophotonics.

Building upon our prior work with BDP0, a NIR dye exhibiting NIR absorption properties and J-aggregation in nanoparticle form, we sought to enhance these characteristics by designing functional dyes with D-A-D structures [23]. This was accomplished by introducing strong electron-donating groups at the 1,7-positions. Specifically, we selected dipropylamine, with its two extended propyl chains, to assess potential impacts on molecular aggregation, and julolidine, recognized for its strong electron-donating capability and planarity, to facilitate intramolecular charge transfer (ICT) and enhance aggregation tendencies [24–27]. Utilizing established synthetic methodologies, reported by O'Shea [28], we synthesized aza-BODIPY derivatives BDP1 and BDP2 (Fig. 1A). The process commenced with the condensation of an aldehyde and 2-acetylthiophene to form chalcone **1**, followed by a Michael addition with nitromethane to yield **2**. Subsequent reflux with ammonium acetate in *n*-butanol produced **3**, which, upon reaction with boron trifluoride etherate in the presence of triethylamine, afforded the target products BDP1 and BDP2. Structural confirmation was obtained through ^{1}H and ^{13}C nuclear magnetic resonance (NMR) spectroscopy as well as high resolution mass spectrometer (HRMS).

Density functional theory (DFT) calculations were employed to optimize the geometries of BDP0 through BDP2, as illustrated in Fig. 1B, Figs. S1 and S2, Tables S1 and S2 (Supporting information) [29]. The C–N bond lengths at the 1,7-positions measured 1.389 Å for BDP1 and 1.382 Å for BDP2, indicating partial double-bond character. A progressive decrease in C–C bond lengths between the 1,7-position benzene ring and the parent nucleus from BDP0 to BDP2 suggested that electron-donating groups at these positions enhance electron delocalization and ICT. Additionally, ground-state dipole moments increased from 1.04 D in BDP0 to 7.89 D in BDP2, reflecting augmented ICT within the donor-acceptor skeleton.

The single crystal of BDP2 was obtained as shown in Fig. 1C. The C–C (1.447 Å) and C–N (1.367 Å) bond lengths within the julolidine substituents were consistent with partial double-bond character, corroborating theoretical predictions. The dihedral angles between julolidine, thiophene units, and the parent nucleus were approximately 25.1° and 21.1°, respectively, facilitating electron delocalization from donor groups to the electron-deficient core. The entire aza-dipyrrin framework exhibited a coplanar tilted arrangement, with a transition dipole moment slip angle of 17.4°, characteristic of J-type aggregates [30,31]. Comparative analysis with BDP0′s reported single-crystal structure [32] indicated that BDP2′s larger julolidine substituents result in an increased average intermolecular distance of approximately 4.10 Å, compared to 2.48 Å in BDP0. This suggests that BDP2 forms looser J-aggregates due to the steric bulk of julolidine. Top-view examination of the crystal stacking showed π-π interactions between the electron-deficient aza-dipyrrin core and adjacent electron-rich thiophene or julolidine groups, with an intermolecular distance of 3.50 Å, indicating weak short-range exciton coupling.

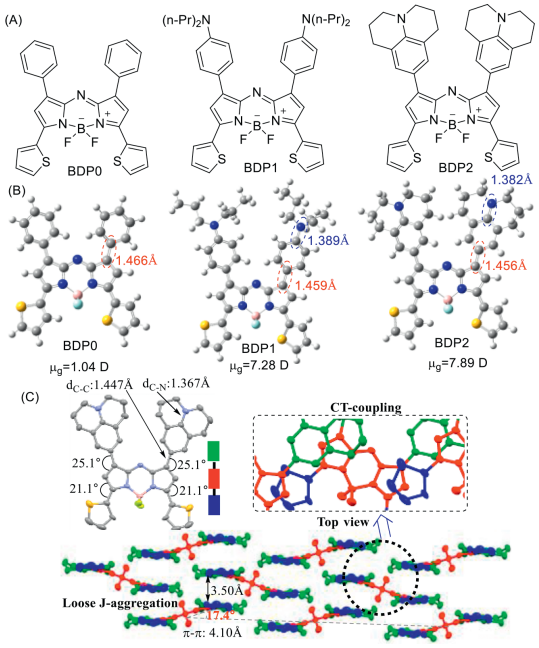


Fig. 1. (A) Structures of BDP0–2. (B) The optimized ground state geometry (S_0 state) calculated at the B3LYP/6–31G(d, p) level. (C) Molecular structure of BDP2 in the single crystal state (light cyan for the F atom, yellow for the S atom, light blue for the N atom, grey for the C atom, pink for the B atom, hydrogen atoms are omitted for clarity) and packing motif in the single-crystal structure (red for core structure, green for julolidine moiety, blue for thiophene moiety).

The optical properties of BDP0, BDP1, and BDP2 were evaluated (Figs. S3 and S4, Table S3 in Supporting information). Unlike BDP0, which shows relatively narrow absorption, BDP1 and BDP2 exhibit broader UV–vis-NIR absorption peaks. In DCM, the maximum absorption peaks of BDP0, BDP1, and BDP2 are observed at 717, 831, and 892 nm, respectively, with molar extinction coefficients (ε) of approximately 10^4 L mol^{-1} cm^{-1}.

The significant red shifts in BDP1 and BDP2 relative to BDP0 are attributed to the introduction of amino groups. The julolidine group in BDP2 further enhances ICT effects [33], particularly on nitrogen, promoting a red shift into the NIR-II region, making it highly suitable for photofunctional research. As solvent polarity increases (*e.g.*, from hexane to DMSO), BDP1 and BDP2 exhibit additional red shifts, consistent with the ICT effect. While BDP0 fluoresces in solution, BDP1 and BDP2 do not, likely due to ICT-driven suppression of radiative decay processes, which enhances their photothermal conversion potential. These photophysical properties position BDP1 and BDP2 as promising photothermal agents for NIR applications.

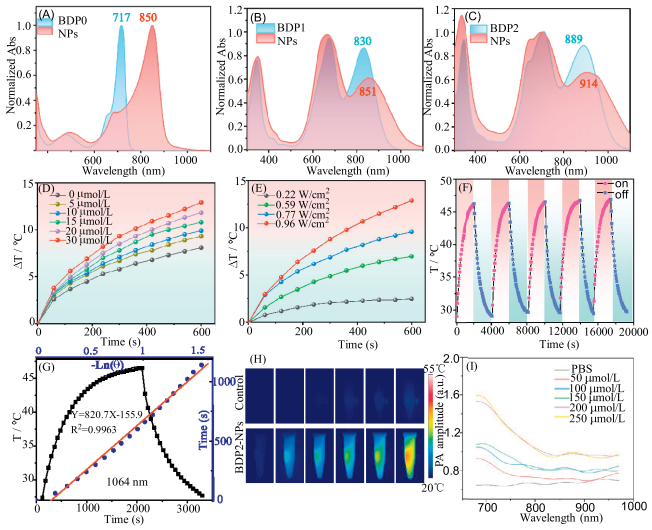


Fig. 2. (A–C) Comparison of the absorption of BDP0–2 in DCM and BDP0–2-NPs in water. (D) Heating curves of the BDP2-NPs at various concentrations upon laser-1064 nm irradiation (0.96 W/cm^2). (E) Heating curves of the BDP2-NPs (30 μmol/L) at increasing power density. (F) Heating and cooling curves of the BDP2-NPs (30 μmol/L) upon five times laser-1064 nm irradiation (0.96 W/cm^2). (G) Heating curves of the BDP2-NPs (30 μmol/L) during a laser-on and off switching process, with the inset showing the related linear cooling time data *versus* $-\ln(\theta)$. $\eta = 34.2\,\%$. (H) Photothermal imaging of the BDP2-NPs at different irradiation times. (I) PA signal spectra of BDP2-NPs at different concentrations of 680–970 nm.

To analyze the impact of amino groups on the absorption spectrum, we conducted hole-electron analysis [34] using Multiwfn 3.8 (dev) [35,36], with results for relevant excited states of BDP0, BDP1, and BDP2 shown in Fig. S2 and Table S2. The hole and electron distributions and the relatively small D index indicate that the S_1 state of BDP0 is a local excitation. The S_1 states of BDP1 and BDP2 exhibit relatively large D indices, with Sr indices only slightly smaller than that of the S_1 state of BDP0. Analysis of the distribution of holes and electrons suggests that these states are primarily charge-transfer excitations with a minor localized excitation feature. In contrast, the S_2 states of BDP1 and BDP2 have smaller Sr indices and larger D indices, further indicating that they are also predominantly charge-transfer excitations. The energy gaps between highest occupied molecular orbital (HOMO) and lowest unoccupied molecular orbital (LUMO) progressively narrow from BDP0 (3.92 eV) to BDP1 (3.78 eV) and BDP2 (3.70 eV), correlating with the red-shifted absorption wavelengths and the enhanced electron-donating properties of the substituted amino groups (Fig. S1 and Table S1).

To improve water solubility, BDP derivatives were modified using the amphiphilic polymer polyethylene-polypropylene glycol (F-127). The resulting BDP0–2 nanoparticles (NPs) displayed red-shifted absorption spectra relative to their DCM solutions, indicative of J-aggregation (Figs. 2A–C, Figs. S5 and S6 in Supporting information). BDP0-NPs exhibited a notable red shift of 143 nm, while BDP1-NPs and BDP2-NPs showed smaller shifts of 20–25 nm, likely due to differences in the size of the amino groups on the 1,7-benzene ring. The absorption spectrum of BDP2-NPs spans the NIR-I region and partial tail-absorption in the NIR-II region. Compared to indocyanine green (ICG), BDP0–2-NPs showed superior photostability (Fig. S5A). To confirm that observed spectral changes were not concentration-dependent, the absorption spectra of BDP2 at varying concentrations were analyzed. The consistent peak shapes and positions across concentrations indicated aggregation behavior in the nanoparticles (Fig. S6). Generally, the red-shifted absorption peak of CT-coupled J aggregation is stronger than the blue-shifted absorption peak, but BDP1–2-NPs shows the opposite trend, which is related to the overlapping of the CT peaks of its single molecules. Given their favorable photostability and NIR absorption, BDP2-NPs were selected for further investigation.

Dynamic light scattering (DLS) analysis revealed that BDP2-NPs have an average hydrodynamic diameter of 103 nm (Fig. S5B). Transmission electron microscopy (TEM) confirmed that BDP2-NPs are spherical and uniform in size, which is advantageous for cellular applications. Importantly, the absorption properties of BDP2-NPs remained stable over seven days of testing, demonstrating excellent photostability (Fig. S5C).

The absence of fluorescence emission from BDP2-NPs prompted an initial investigation of their potential to generate singlet oxygen. Diphenylisobenzofuran (DPBF) was used as a probe for singlet oxygen detection. Upon illumination with an 808 nm light source for 20 s, a slight reduction in DPBF absorbance at 418 nm was observed, confirming the generation of singlet oxygen. However, exposure to a 1064 nm laser resulted in minimal singlet oxygen production (Fig. S7 in Supporting information). These results suggest that while BDP2-NPs can produce small amounts of singlet oxygen.

The combination of NIR-I/II absorption, fluorescence suppression, and limited singlet oxygen production led to an evaluation of the photothermal properties of BDP2-NPs (Figs. 2D–H). Under 1064 nm light irradiation, the photothermal conversion efficiency of BDP2-NPs showed a concentration-dependent increase in temperature (Fig. 2D). For instance, at 0.96 W/cm^2, the temperature rose by 13 °C within 10 min, compared to only a 7 °C increase for water under identical conditions. Additionally, the photothermal effect of BDP2-NPs was directly proportional to laser power density and illumination time (Figs. 2E and H). Based on the temperature change during the cooling phase [37], the photothermal conversion efficiency was calculated to be 34.2 % (Fig. 2G), highlighting the potential of BDP2-NPs for tumor PTT. Moreover, after five cycles of light irradiation heating and natural cooling (Fig. 2F), the temperature change of BDP2-NPs nanoparticles was almost unaffected, indicating that BDP2-NPs nanoparticles possess exceptional photothermal stability. When exposed to 808 nm laser irradiation, BDP2-NPs exhibited similar trends of concentration- and power-dependent temperature increases. Under test conditions (30 μmol/L, 0.96 W/cm^2), the temperature reached 55 °C, with a photothermal conversion efficiency of 48.4 % (Fig. S8 in Supporting information). These results underline the robust photothermal performance and stability of BDP2-NPs, which are critical for cancer therapy. The photothermal properties of BDP2-NPs are inherently linked to their PA capabilities. Photothermal nanoparticles convert absorbed photon energy into heat, generating ultrasound waves through thermoelastic expansion and pressure fluctuations. BDP2-NPs produced clear PA signals under 680–970 nm, with signal intensity increasing consistently with nanoparticle concentration (0–250 μmol/L) (Fig. 2I). These findings indicate that BDP2-NPs have potential as PA contrast agents for imaging-guided tumor phototherapy.

To assess the biocompatibility and phototoxicity of BDP2-NPs, MTT assays were performed on HCT-116 and CT-26 tumor cells (Fig. 3A). In the absence of light, BDP2-NPs exhibited negligible cytotoxicity, with cell viability remaining high even at a concentration of 30 μmol/L, indicating excellent biocompatibility. However, under 1064 nm light irradiation (100 mW/cm^2, 5 min), cell viability decreased significantly with increasing BDP2-NPs concentration, demonstrating strong phototoxicity. Overall, these resulting indicate that BDP2-NPs possess a strong phototherapeutic effect and good phototoxicity towards tumor cells. To balance the desired therapeutic effect and minimize potential cytotoxicity, an appropriate probe concentration of 10 μmol/L was chosen for subsequent experiments.

Despite the limited singlet oxygen generation capacity of BDP2-NPs in solution, their photodynamic impact on tumor cells was

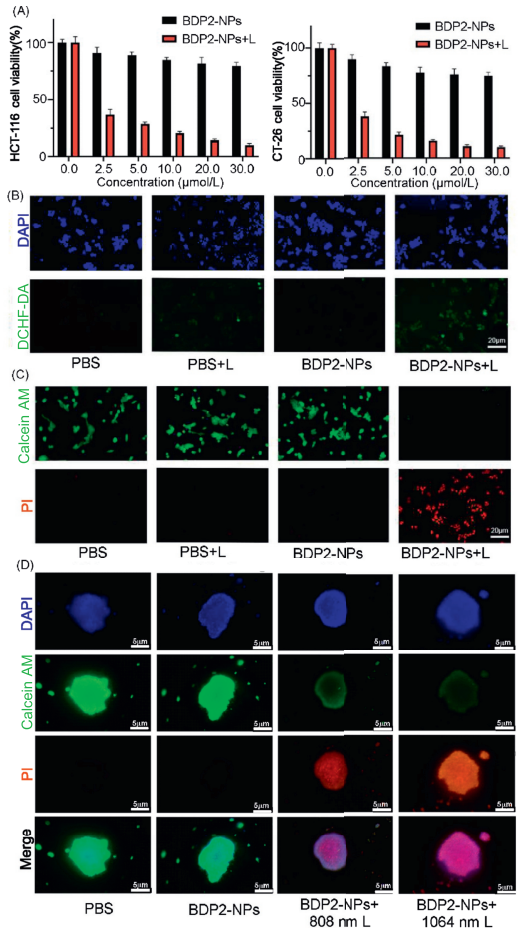


Fig. 3. (A) MTT assay for HCT-116/CT-26 cells after treatment with BDP2-NPs at different concentrations in the presence (laser) and absence (dark) of irradiation. Data are presented as mean ± standard deviation (SD) ($n = 5$). (B) Examination of the photodynamic properties of probes. Laser: 1064 nm laser irradiation for 5 min (100 mW/cm^2). (C) Fluorescence microscope imaging of apoptosis of cancer cells induced by laser irradiation of BDP2-NPs. Laser: 1064 nm laser irradiation for 5 min (100 mW/cm^2). Scale bar: 20 μm. (D) Therapeutic efficacy of BDP2-NPs against 3D tumor spheroids. 808 nm L: 808 nm laser, 100 mW/cm^2, 5 min; 1064 nm L: 1064 nm laser, 100 mW/cm^2, 5 min. Scale bar: 5 μm.

evaluated. 2′,7′-Dichlorofluorescein diacetate (DCFH-DA) was used as a fluorescent probe to detect reactive oxygen species (ROS) in HCT-116 cells (Fig. 3B). DCFH-DA reacts with intracellular ROS to form 2′,7′-dichlorofluorescein (DCF), which fluoresces green upon excitation at 488 nm. Among the tested groups, phosphate buffered saline (PBS), PBS + L (light only), and BDP2-NPs + L, only the BDP2-NPs + L group exhibited weak green fluorescence, indicating low levels of ROS generation under 1064 nm irradiation. These findings confirm that BDP2-NPs mediate minimal intracellular ROS production during photodynamic therapy.

To further explore the phototherapeutic potential of BDP2-NPs, live-dead cell staining was performed under 1064 nm light irradiation (100 mW/cm^2) (Fig. 3C). Propidium iodide (PI) dye (red) marked dead cells, while calcein-AM (green) labeled live cells. Intense red fluorescence was observed in the BDP2-NPs + L group, signifying near-total elimination of HCT-116 cells following laser irradiation (100 mW/cm^2, 5 min). Conversely, robust green fluorescence was detected in the PBS, PBS + L, and BDP2-NPs groups, confirming the biocompatibility of BDP2-NPs in the absence of light. These results demonstrate the strong photothermal capability of BDP2-NPs to effectively eliminate tumor cells under NIR-II laser irradiation. Flow cytometry analysis further supported these findings (Fig. S9 in Supporting information), showing cell viability exceeding 80 % in the BDP2-NPs group under dark conditions, with a marked reduction following laser treatment, consistent with fluorescence imaging results.

Given the strong and broad absorption spectrum of BDP2-NPs, we investigated the potential of dyes for deep tissue PA imaging by simulating tissue thickness using chicken breast. 100 μmol/L nanoparticle solution were placed in a capillary PA tube, covered with approximately 10 mm of chicken breast tissue, and different excitation wavelengths were used to assess the PA imaging capability of various nanoparticles. As shown in Figs. S10 and S11 (Supporting information), BDP0-NPs and BDP1-NPs produced relatively weak PA signals under ~10 mm of tissue, slightly surpassing the PBS control. In contrast, BDP2-NPs exhibited significantly stronger PA signals across all tested wavelengths. These results suggest that BDP2-NPs offer superior tissue penetration depth and robust PA imaging capabilities in both the NIR-I and NIR-II regions. Additionally, they can be matched with most laboratory laser wavelengths for tumor ablation experiments, showing great potential in antitumor research and applications.

As shown in the Fig. 3D, 3D tumor spheroids were stained with 4′,6-diamidino-2-phenylindole (DAPI) (blue), calcein-AM (green), and PI (red) to assess cell viability after various treatments. The PBS and BDP2-NPs-only groups exhibited strong calcein-AM signals and negligible PI staining, indicating high cell viability and minimal cytotoxicity. Upon irradiation with 808 nm laser following BDP2-NPs incubation, increased PI fluorescence and reduced calcein-AM signal were observed, suggesting partial photothermal-induced cell death. Notably, the BDP2-NPs + 1064 nm laser group showed the strongest PI signal and the weakest calcein-AM fluorescence, indicating extensive cell death and enhanced PTT efficacy under 1064 nm irradiation. These observations highlight the superior PTT efficacy of BDP2-NPs under 1064 nm laser irradiation compared to 808 nm. This enhancement can be attributed not only to the intrinsic photothermal performance of BDP2-NPs at this wavelength but also to the deeper tissue penetration capability of the 1064 nm laser. Given the lower scattering and absorption of biological tissues in the NIR-II region, 1064 nm irradiation is more effective in delivering energy to the inner regions of the 3D tumor spheroids, thereby inducing more extensive tumor cell death. These findings suggest that 1064 nm laser excitation offers a promising advantage for *in vivo* applications, particularly in treating deep-seated tumors.

In this study, we developed a novel NIR-II photothermal agent, BDP2, and its nanoparticle formulation, BDP2-NPs, based on the aza-BODIPY platform with a D-A-D structure. BDP2-NPs exhibit efficient tail absorption beyond 1000 nm, coupled with low dark toxicity, high phototoxicity, and excellent biocompatibility. Under 1064 nm excitation, these nanoparticles achieve a photothermal conversion efficiency of 34.2 % and a maximum temperature increase of up to 47 °C, as well as excellent PA imaging, demonstrating controlled and effective photothermal performance. These findings underscore the promise of aza-BODIPY-based dyes as mild yet potent NIR-II PA imaging and photothermal agents for cancer therapy, paving the way for further advancements in photothermal treatment strategies.

Declaration of competing interest

The authors declare that they have no known competing financial interests or personal relationships that could have appeared to influence the work reported in this paper.

CRediT authorship contribution statement

Siyi Hu: Validation, Project administration. **Wenze Zhang:** Investigation, Data curation. **Zhigang Ni:** Formal analysis, Data cu-

ration. **Liang Tian:** Investigation. **Jiangwei Tian:** Writing – original draft, Supervision. **Hua Lu:** Writing – review & editing, Supervision. **Lizhi Gai:** Writing – original draft, Supervision.

Acknowledgments

We thank the National Natural Science Foundation of China (No. 22471051) and the Fundamental Research Funds for the Central Universities (No. 2632024TD05) for financial support. The Interdisciplinary Research Project of Hangzhou Normal University (No. 2024JCXK01) for supporting this work. Theoretical calculations were carried out at the Computational Centre for Molecular Design of Organosilicon Compounds, Hangzhou Normal University.

Supplementary materials

Supplementary material associated with this article can be found, in the online version, at doi:10.1016/j.cclet.2025.111523.

References

[1] C. Kim, C. Favazza, L.V. Wang, Chem. Rev. 110 (2010) 2756–2782.
[2] A.B.E. Attia, G. Balasundaram, M. Moothanchery, et al., Photoacoustics 16 (2019) 100144.
[3] L.V. Wang, S. Hu, Science 335 (2012) 1458–1462.
[4] Z. Li, J. Cheng, P. Huang, G. Wu, W. Lin, Chin. Chem. Lett. 35 (2024) 109153.
[5] A.M. Smith, M.C. Mancini, S. Nie, Nat. Nanotechnol. 4 (2009) 710–711.
[6] S. He, J. Song, J. Qu, Z. Cheng, Chem. Soc. Rev. 47 (2018) 4258–4278.
[7] A.L. Antaris, H. Chen, K. Cheng, et al., Nat. Mater. 15 (2016) 235–242.
[8] Y.Duan Kenry, B. Liu, Adv. Mater. 30 (2018) 1802394.
[9] H.S. Choi, H.K. Kim, Nat. Biomed. Eng. 4 (2020) 245–246.
[10] S. Gai, G. Yang, P. Yang, et al., Nano Today 19 (2018) 146–187.
[11] Z. Lei, F. Zhang, Angew. Chem. Int. Ed. 60 (2021) 16294–16308.
[12] Y. Liu, Y. Li, S. Koo, et al., Chem. Rev. 122 (2021) 209–268.
[13] J.S.D. Mieog, F.B. Achterberg, A. Zlitni, et al., Nat. Rev. Clin. Oncol. 19 (2022) 9–22.
[14] G. Hong, A.L. Antaris, H. Dai, Nat. Biomed. Eng. 1 (2017) 0010.
[15] L. Wang, A. Mei, N. Li, et al., Chin. Chem. Lett. 35 (2024) 108974.
[16] Q. Sun, H. Liu, Y. Yang, et al., Chem. Biomed. Imaging 3 (2025) 260–266.
[17] K. Song, H. Gao, X. Wang, Z. Liu, ChemPhotoChem 9 (2025) e202400335.
[18] X. Hu, C. Zhu, F. Sun, et al., Adv. Mater. 36 (2024) 2304848.
[19] K. Li, X. Duan, Z. Jiang, et al., Nat. Commun. 12 (2021) 2376.
[20] X. Hu, Z. Fang, C. Zhu, et al., Adv. Funct. Mater. 34 (2024) 2401325.
[21] J.H. Kim, T. Schembri, D. Bialas, M. Stolte, F. Würthner, Adv. Mater. 34 (2022) 2104678.
[22] S. Lv, X. Gong, Y. Xue, et al., Chin. Chem. Lett. 37 (2026) 111171.
[23] S. Wu, W. Zhang, C. Li, et al., Chem. Sci. 15 (2024) 5973–5979.
[24] H. Chen, B. Dong, Y. Tang, W. Lin, Acc. Chem. Res. 50 (2017) 1410–1422.
[25] Z. Shi, H. Bai, J. Wu, et al., Research 19 (2023) 0169.
[26] L. Bai, P. Sun, Y. Liu, et al., Chem. Commun. 55 (2019) 10920–10923.
[27] L. Cao, Y. Li, D. Zhang, et al., Chin. Chem. Lett. 35 (2024) 109735.
[28] C.W. Bird, J. Lu, Tetrahedron Lett. 33 (1992) 7253–7254.
[29] M.J. Frisch, G.W. Trucks, H.B. Schlegel, et al., Gaussian 16, Revision C.01, Gaussian, Inc., Wallingford CT, 2019.
[30] E.E. Jelley, Nature 138 (1936) 1009–1010.
[31] T.E. Kaiser, H. Wang, V. Stepanenko, F. Würthner, Angew. Chem. Int. Ed. 46 (2007) 5541–5544.
[32] X. Zhang, H. Yu, Y. Xiao, J. Org. Chem. 77 (2012) 669–673.
[33] J.M. Fisher, J.P. O'Connor, P.J. Brown, et al., J. Phys. Chem. A 127 (2023) 2946–2957.
[34] Z. Liu, T. Lu, Q. Chen, Carbon 165 (2020) 461–467.
[35] T. Lu, F. Chen, J. Comput. Chem. 33 (2012) 580–592.
[36] T. Lu, J. Chem. Phys. 161 (2024) 082503.
[37] D.K. Roper, W. Ahn, M. Hoepfner, J. Phys. Chem. C 111 (2007) 3636–3641.